optica

Polarization contrast of nanoscale waveguides in high harmonic imaging

Sergey Zayko, Murat Sivis, Sascha Schäfer, and Claus Ropers*

4th Physical Institute: Solids and Nanostructures, University of Göttingen, 37077 Göttingen, Germany
Corresponding author: cropers@gwdg.de

The optical polarization response of a structured material is one of its most significant properties, carrying information about microscopic anisotropies as well as chiral features and spin orientations. Polarization analysis is therefore a key element of imaging and spectroscopy techniques throughout the entire spectrum. In the case of extreme ultraviolet (EUV) radiation, however, both the preparation and detection of well-defined polarization states remain challenging. As a result, polarization-sensitive EUV microscopy based on table-top sources has not yet been realized, despite its great potential, for example, in nanoscale magnetic imaging. Here, we demonstrate polarization contrast in coherent diffractive imaging using high harmonic radiation and investigate the polarization properties of nanoscale transmission waveguides. We quantify the achievable polarization extinction ratio for different waveguide geometries and wavelengths. Our results demonstrate the utility of slab waveguides for efficient EUV polarization control and illustrate the importance of considering polarization contrast in the imaging of nanoscale structures. © 2016 Optical Society of America

High harmonic generation (HHG) yielding coherent extreme ultraviolet (EUV) radiation at laboratory scales has extended the frontiers of ultrafast spectroscopy and imaging to attosecond temporal resolution [1]. Recently, novel schemes leading to efficient HHG sources with elliptical [2,3] and circular [4–6] polarizations highlighted the potential for studying polarization-sensitive light–matter interactions, as demonstrated in HHG-based measurements of circular dichroism [5,7,8]. More generally, the polarization state of high harmonic radiation is naturally expected to affect the signal and contrasts in various techniques, such as coherent diffractive imaging (CDI) [9–11], holography [12], and attosecond spectroscopy [13]. Besides the generation of EUV light with defined polarization, crucial aspects for polarization-dependent imaging and spectroscopy are the control and determination of a given polarization state. Due to the lack of suitable

materials exhibiting high optical transmissivity at EUV wavelengths, most approaches used to manipulate and measure polarization in this spectral range rely on reflective components, such as multilayer mirrors or gratings. However, these components are often limited to a rather narrow spectral range, require precise alignment, and inevitably influence the direction of light propagation, which imposes additional constraints. Therefore, alternative strategies for polarization control, e.g., in transmission schemes, are highly desirable, and nanostructured materials harnessing EUV waveguiding may be a promising approach [14,15].

Here, we investigate polarization effects in EUV light propagation through nanoscale slab waveguides by means of HHG-based coherent diffractive imaging, and we discuss the capabilities of these structures to serve as transmission polarizers. Specifically, the light transmitted through the waveguides is analyzed in far-field diffraction, and a phase retrieval algorithm is used to reconstruct the exit wave. We find a strong polarization anisotropy of the waveguide propagation, with enhanced transmission for polarization parallel to the waveguides (TE mode), and observe a polarization contrast that depends on the incident wavelength. A compact linear polarization analyzer is realized by arranging slits with different orientations and mapping the incident polarization into angle-dependent diffraction intensities within a single acquisition. Representing the first demonstration of polarization contrast in lensless imaging using HHG, our results highlight the potential of CDI for the study of locally and microscopically anisotropic and chiral structures.

The schematic of the experimental setup is depicted in Fig. 1. A table-top HHG source provides linearly polarized coherent radiation at odd harmonics of the driving laser frequency (amplified 40 fs Ti:sapphire laser pulses, 800 nm central wavelength). Single harmonics in a wavelength range from 28 to 42 nm (29th to 19th harmonic order) are selected and focused by a combination of a blazed toroidal diffraction grating and a motorized slit, resulting in quasi-monochromatic, vertically polarized illumination conditions in the sample plane. The sample (see Fig. 1) is placed in the EUV focus, and the transmitted light scattered from the nanostructure is collected by a CCD camera with a high numerical aperture. The sample orientation is adjusted normal to the HHG beam with a precision better than 0.5° using the back reflection of an alignment laser. From the recorded far-field diffraction pattern, the exit wave behind the object is reconstructed with diffraction-limited resolution. Further details on
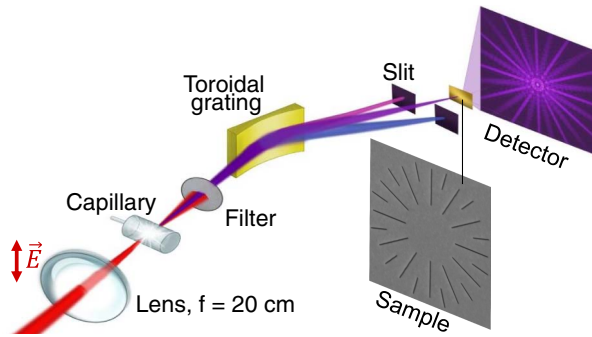
Fig. 1. Schematic of the experimental setup. High harmonics are generated by focusing femtosecond laser pulses into an argon-filled capillary. After passage through an aluminum filter (150 nm), a single harmonic is focused onto the sample by a toroidal diffraction grating. A CCD camera collects diffraction images from the waveguide structures.

the HHG setup and beam characterizations are described elsewhere [14,16].

The samples are produced by the focused ion beam etching of 200-nm-thick silicon nitride (Si_3N_4) membranes coated with 140 nm of gold film. Rectangular slits are milled into the samples, resulting in hollow waveguides with high aspect ratios in both the transverse and longitudinal directions (slit length larger than 1 μm, slit widths w of few tens of nanometers, depth of $L = 340$ nm). To investigate the polarization dependence of EUV transmission through the waveguides, we designed a pattern with a clock-like arrangement of 50-nm-wide slits, as shown in the scanning electron microscope (SEM) image in Fig. 2(a). Employing linear incident polarization [vertical in Fig. 2(c)], within a single diffraction pattern, different slit orientations yield direct access to the transmission intensity as a function of the angle between the polarization axis and the waveguides. Due to the high EUV absorption of the materials used, the transmission through the nonetched regions is below 10^{-10}, such that only waveguide transmission contributes to the signal.

Figure 2(b) shows the far-field diffraction intensity (logarithmic scale) recorded at a distance of 25 mm behind the sample and for illumination with a wavelength of 35 nm (23rd harmonic). Sufficient oversampling [11] in the diffraction pattern allows for a reconstruction of the field amplitudes and phases of the exit

wave. We use the relaxed averaged alternating reflection algorithm [17] and apply it to the diffraction pattern together with an autocorrelation-based real space support obtained from the inverse Fourier transform of the diffraction pattern. Figure 2(c) displays the reconstructed exit wave intensity, which is in close agreement with the overall shape of the structure. The objects studied are significantly smaller than both the focus diameter and the lateral wavefront distortions, as determined from previous beam characterizations [16]. Therefore, the current conditions essentially correspond to plane wave illumination, and the reconstructed exit wave represents the complex transmission functions of each individual waveguide in a single reconstructed image. As is apparent from Fig. 2(c), the reconstructed exit wave intensities are strongly dependent on the slit orientation. Specifically, the vertical waveguides, i.e., those parallel to the incident polarization, are noticeably brighter than the horizontal ones. The same behavior is evident also in the diffraction pattern, taking into account that the far field is composed of a superposition of diffracted exit wave fields from pairs of elongated rectangular apertures. Each of the slit pairs contributes a diffraction streak in the respective perpendicular direction. Specifically, following standard diffraction theory [18], the extended length of the diffraction streaks in reciprocal space is governed by the strong confinement from the narrow waveguide width, the widths of the streaks are determined by the length of the individual slits, and double-slit interference between slits of the same orientation cause a fine sinusoidal modulation of the streaks. At high spatial frequencies, the streaks from differently oriented slits are particularly well separated.

In Fig. 2(d), the integrated exit wave (red circles) and the far-field (blue triangles) intensities (normalized to the length of the individual waveguides) in the reconstruction and the diffraction pattern, respectively, are plotted as a function of the slit orientation angle θ. Here, θ is defined as ranging from 0 to 2π, corresponding to the full circle of slits. The high reproducibility of the fabrication is evident from the nearly identical signals measured for each of the four equivalent slit orientations with equal $mod(|\theta|, \pi)$, e.g., $\theta = \pm n \cdot 15°$ and $\theta = 180° \pm n \cdot 15°$ with integer n. Because of the inversion symmetry of the diffraction streaks in Fig. 2(b), both opposing parts of each feature are combined, such that the blue symbols in Fig. 2(d) are only plotted from 0 to π. The normalized experimental data points evaluated from the diffraction pattern and the reconstruction agree with the
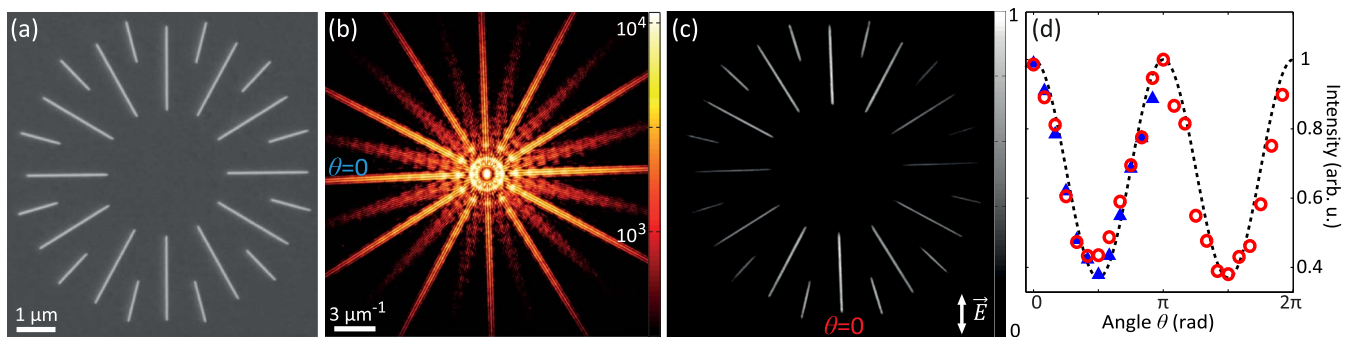

Fig. 2. Demonstration of polarization contrast in CDI. (a) Scanning electron micrograph of a sample carrying a clock-like arrangement of slab waveguides. (b) Recorded diffraction pattern at 35 nm wavelength. (c) Reconstructed exit wave intensity obtained by iterative phase retrieval. The angle-dependent intensity variation reflects the polarization contrast in transmission (incident polarization: vertical). (d) Transmitted intensity plotted as a function of the slit orientation angle θ [$\theta = 0$ corresponds to the vertical waveguide in the bottom of (c)]. Red circles: Intensity evaluated from the exit wave reconstruction. Blue triangles: Intensity obtained directly from the diffraction pattern. Dashed line: Fit to the behavior of an imperfect polarizer (see text).
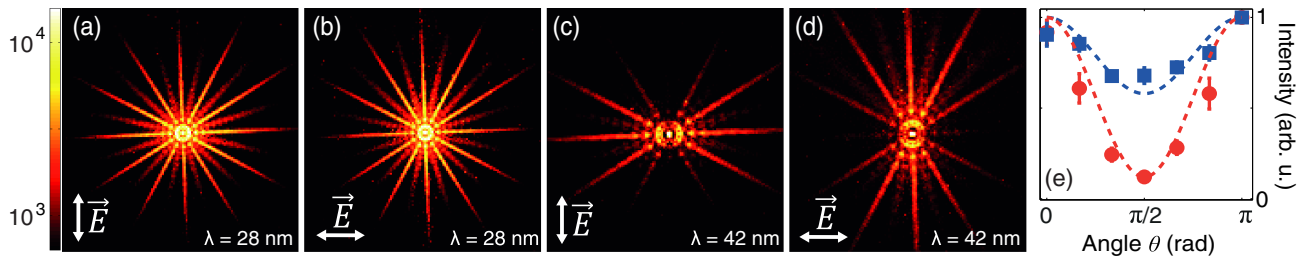
Fig. 3. Wavelength dependence of polarization contrast. (a)–(d) Far-field diffraction images of the object from Fig. 2 for different polarization angles [(a), (c): vertical; (b), (d): horizontal)] and wavelengths λ. (e) Transmission as a function of waveguide orientation θ (evaluated for vertical polarization) at $\lambda = 28$ nm (blue) and 42 nm (red), showing increased contrast at longer wavelengths.

expectation of an imperfect polarizer [Malus law, black dashed line in Fig. 2(d)]: $I_{tr}(\theta) = \cos^2\theta + C \cdot \sin^2\theta$, where $C = I_{\min}/I_{\max} = 1\!:\!2.7$ is the polarization extinction ratio between the maximum and minimum transmissions.

The achievable extinction ratio will depend on the illuminating wavelength as well as the waveguide properties, such as the width, propagation length, and the cladding materials. In order to study such dependencies and identify conditions with a higher contrast, we have performed measurements using different illumination wavelengths and narrower waveguides. As the converged exit wave reconstruction and the diffraction data yielded the same polarization contrast, in the following, we limit the discussion to direct evaluations of the diffraction data.

Figures 3(a)–3(d) show a set of far-field diffraction patterns obtained for vertical and horizontal incident polarizations (indicated by arrows) and at illumination wavelengths of 28 nm [(a), (b)] and 42 nm [(c), (d)]. The normalized transmitted intensity is plotted in Fig. 3(e) as a function of θ [evaluated from Figs. 3(a) and 3(c)], displaying a strong increase of polarization contrast with wavelength, which reaches 1:1.5 and 1:8 at wavelengths of 28 and 42 nm, respectively.
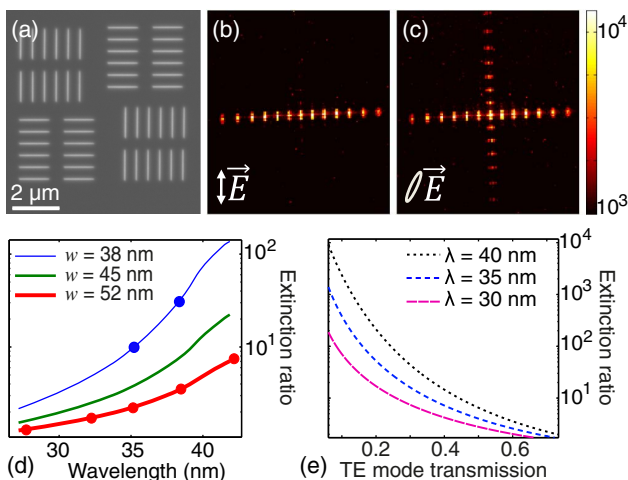

Fig. 4. (a) SEM image of a structure with two orthogonal slit orientations. (b), (c) Diffraction pattern recorded at $\lambda = 38$ nm for vertical (c) and elliptical (d) polarization, indicated by the tilted ellipse (see text). (d) Solid lines: Simulated extinction ratios as a function of λ for different slit widths w in the double-layer geometry of the experiments. Circles: Experimentally determined extinction ratios for the structures in Fig. 2 (red) and Fig. 3 (blue). (e) Simulated polarization contrast of a 300-nm-deep gold waveguide as a function of TE mode transmission.

We investigated the influence of the waveguide width on the extinction ratio by using a second structure composed of narrower waveguides [cf. SEM image in Fig. 4(a)]. The pattern contains 40-nm-wide waveguides (estimated from SEM characterization) with only two perpendicular slit orientations. This configuration is chosen to increase the transmittance of the structure and allows for an evaluation of the polarization contrast with an improved signal-to-noise ratio. Figure 4(b) depicts a diffraction pattern (logarithmic intensity scale) obtained with $\lambda = 38$ nm radiation and vertical incident polarization. A high polarization contrast of $C = 1\!:\!(28 \pm 1)$ is found, with the maximum diffraction intensity again stemming from the vertical slits (corresponding to TE-mode transmission, in which the electric field is parallel to the waveguide walls). For comparison, Fig. 4(c) displays a diffraction pattern recorded after the rotation of the polarization of the HHG pump beam by 30°, which (after grating reflection) results in a weakly elliptical polarization (ellipse indicated) and therefore increased diffraction from the horizontal waveguides.

In order to quantitatively model our results, we theoretically treat the light propagation through the nanoscale waveguides within a modal expansion. Specifically, we solve Maxwell's equations for the TE and TM modes in gold- and Si_3N_4-coated vacuum-core slab waveguides, obtaining complex propagation constants $\beta_{TE/TM}(\lambda, L)$ as a function of the wavelength and waveguide width. For the aspect ratios given (depth versus width), the transmission is governed primarily by the fundamental mode, while higher-order modes are absorbed [14]. Assuming equal incoupling to the waveguide by both polarizations, the polarization extinction ratio is determined by the imaginary parts of the propagation constants and the waveguide thickness as follows: $C = \exp(-2 \cdot \text{Im}(\beta_{TM} - \beta_{TE}) \cdot L)$. The origin of higher TE transmission compared to TM transmission, something previously found at longer UV wavelengths [15,19], should be discussed. This observation is opposite to what is widely found in metallic wire-grid polarizers at visible and infrared wavelengths [18]. These devices employ the fact that there is a cutoff for TE polarization (but not for TM polarization) at sub-wavelength widths and for high-conductivity cladding. At EUV wavelengths, on the other hand, the materials used exhibit high absorption. Thus, the enhanced Fresnel reflection coefficients of TE compared to TM polarization at the waveguide walls is responsible for the polarization contrast. Narrower waveguides involve higher effective propagation angles [18], such that high contrasts are achieved even for waveguides wider than the wavelength.

For our waveguides composed of two materials (200 nm of Si_3N_4 and 140 nm of gold), the propagation constants were

individually computed. In the case of perfect mode overlap at the transition from gold to Si_3N_4 cladding, the overall polarization contrast follows as the product from both layers. Finite element calculations [20] showed this to be a good approximation for our geometries, and were also in quantitative agreement with the modal expansion regarding the total transmission and polarization extinction ratio. Figure 4(d) plots the polarization extinction ratio of the two structures investigated (circles) as a function of the illuminating wavelength in comparison with the simulation results for different waveguide widths. The curves illustrate the strong increase in contrast for longer wavelengths and narrower waveguides. A very good agreement between the experimental and simulated extinction ratios is found for widths of 52 nm (patterns in Figs. 2 and 3) and 38 nm (pattern in Fig. 4), which is consistent with the SEM width characterization.

The increase of the polarization contrast with wavelength is caused by both higher absorption losses for stronger mode confinement, and more importantly in the case of gold, the wavelength dependence of the refractive index. For a fixed wavelength, the polarization contrast can be further increased at the expense of the total transmission by tuning the waveguide width and depth. Figure 4(e) shows the simulated polarization contrast of 300-nm-long gold waveguides for different illuminating wavelengths as a function of the TE mode transmission that results from varying the waveguide width. The simulations highlight the potential for polarization control in the EUV spectral range with waveguide-based structures. For example, at a wavelength of 40 nm, the polarization contrast exceeds 30 dB at a TE mode transmission of 0.15 (corresponding to a 37 nm waveguide width). Large-area structures with similar aspect ratios can be readily produced using state-of-the art nanolithography and chemical etching [21]. Such structures present a compact alternative to existing schemes for HHG polarization characterization [2,8,22]. Combined with reflective waveplates, this approach may also yield the complete state of polarization. We note that both the overall waveguide transmission and in particular the extinction ratios are weak functions of the incidence angle, rendering these structures suitable for applications with beam tilts or divergences of at least 10°.

In conclusion, we investigated the polarization-dependent EUV light propagation in nanometric slab waveguides using HHG-based lensless imaging and far-field diffraction. The experimentally measured polarization extinction ratios were in close agreement to the theoretical predictions, evidencing the suitability of waveguide arrays in future polarization-sensitive imaging and spectroscopy applications. More generally, our results demonstrate the feasibility of polarization contrast microscopy in the extreme ultraviolet region using laboratory-scale sources. The further development of birefringent transmission waveguides may enable comprehensive polarization control for applications such as magnetic and chiral imaging.

REFERENCES

1. P. B. Corkum and F. Krausz, Nat. Phys. **3**, 381 (2007).
2. X. Zhou, R. Lock, N. Wagner, W. Li, H. C. Kapteyn, and M. M. Murnane, Phys. Rev. Lett. **102**, 073902 (2009).
3. A. Ferré, C. Handschin, M. Dumergue, F. Burgy, A. Comby, D. Descamps, B. Fabre, G. A. Garcia, R. Géneaux, L. Merceron, E. Mével, L. Nahon, S. Petit, B. Pons, D. Staedter, S. Weber, T. Ruchon, V. Blanchet, and Y. Mairesse, Nat. Photonics **9**, 93 (2015).
4. A. Fleischer, O. Kfir, T. Diskin, P. Sidorenko, and O. Cohen, Nat. Photonics **8**, 543 (2014).
5. D. Hickstein, F. Dollar, P. Grychtol, J. Ellis, R. Knut, C. Hernández-García, D. Zusin, C. Gentry, J. Shaw, T. Fan, K. Dorney, A. Becker, A. Becker, H. Kapteyn, M. Murnane, and C. Durfee, Nat. Photonics **9**, 743 (2015).
6. H. Eichmann, A. Egbert, S. Nolte, C. Momma, B. Wellegehausen, W. Becker, S. Long, and J. K. McIver, Phys. Rev. A **51**, R3414 (1995).
7. G. Lambert, B. Vodungbo, J. Gautier, B. Mahieu, V. Malka, S. Sebban, P. Zeitoun, J. Luning, J. Perron, A. Andreev, S. Stremoukhov, F. Ardana-Lamas, A. Dax, C. P. Hauri, A. Sardinha, and M. Fajardo, Nat. Commun. **6**, 6167 (2015).
8. O. Kfir, P. Grychtol, E. Turgut, R. Knut, D. Zusin, D. Popmintchev, T. Popmintchev, H. Nembach, J. M. Shaw, A. Fleischer, H. Kapteyn, M. Murnane, and O. Cohen, Nat. Photonics **9**, 99 (2015).
9. A. Ravasio, D. Gauthier, F. R. N. C. Maia, M. Billon, J. Caumes, D. Garzella, M. Géléoc, O. Gobert, J.-F. Hergott, A.-M. Pena, H. Perez, B. Carré, E. Bourhis, J. Gierak, A. Madouri, D. Mailly, B. Schiedt, M. Fajardo, J. Gautier, P. Zeitoun, P. H. Bucksbaum, J. Hajdu, and H. Merdji, Phys. Rev. Lett. **103**, 028104 (2009).
10. A. Tripathi, J. Mohanty, S. H. Dietze, O. G. Shpyrko, E. Shipton, E. E. Fullerton, S. S. Kim, and I. McNulty, Proc. Natl. Acad. Sci. **108**, 13393 (2011).
11. J. Miao, T. Ishikawa, I. K. Robinson, and M. M. Murnane, Science **348**, 530 (2015).
12. S. Eisebitt, J. Lüning, W. Schlotter, M. Lörgen, O. Hellwig, W. Eberhardt, and J. Stöhr, Nature **432**, 885 (2004).
13. A. L. Cavalieri, N. Muller, T. Uphues, V. S. Yakovlev, A. Baltuska, B. Horvath, B. Schmidt, L. Blumel, R. Holzwarth, S. Hendel, M. Drescher, U. Kleineberg, P. M. Echenique, R. Kienberger, F. Krausz, and U. Heinzmann, Nature **449**, 1029 (2007).
14. S. Zayko, E. Mönnich, M. Sivis, D.-D. Mai, T. Salditt, S. Schäfer, and C. Ropers, Opt. Express **23**, 19911 (2015).
15. M. Gruntman, Appl. Opt. **34**, 5732 (1995).
16. T. Mey, S. Zayko, C. Ropers, B. Schäfer, and K. Mann, Opt. Express **23**, 15310 (2015).
17. D. R. Luke, Inverse Probl. **21**, 37 (2005).
18. B. E. Saleh and M. C. Teich, *Fundamentals of Photonics* (Wiley, 1991), Vol. 22.
19. E. E. Scime, E. H. Anderson, D. J. McComas, and M. L. Schattenburg, Appl. Opt. **34**, 648 (1995).
20. COMSOL Multiphysics 4.4 software suite (wave optics module), Comsol Inc.
21. C. Chang and A. Sakdinawat, Nat. Commun. **5**, 4243 (2014).
22. A. Camper, A. Ferré, V. Blanchet, F. Burgy, D. Descamps, S. Petit, T. Ruchon, and Y. Mairesse, Opt. Lett. **40**, 5387 (2015).